

Probing the circumgalactic medium of active galactic nuclei with background quasars

Glenn G. Kacprzak,^{1,2*} Christopher W. Churchill,³ Michael T. Murphy,¹ Jeff Cooke¹

¹ Centre for Astrophysics and Supercomputing, Swinburne University of Technology, PO Box 218, Victoria 3122, Australia

² Australian Research Council Super Science Fellow

³ Department of Astronomy, New Mexico State University, Las Cruces, NM 88003

ABSTRACT

We performed a detailed study of the extended cool gas, traced by MgII absorption [$W_r(2796) \geq 0.3 \text{ \AA}$], surrounding 14 narrow-line active galactic nuclei (AGNs) at $0.12 \leq z \leq 0.22$ using background quasar sight-lines. The background quasars probe the AGNs at projected distances of $60 \leq D \leq 265 \text{ kpc}$. We find that, between $100 \leq D \leq 200 \text{ kpc}$, AGNs appear to have lower MgII gas covering fractions ($0.09^{+0.18}_{-0.08}$) than quasars ($0.47^{+0.16}_{-0.15}$) and possibly lower than in active field galaxies ($0.25^{+0.11}_{-0.09}$). We do not find a statistically significant azimuthal angle dependence for the MgII covering fraction around AGNs, though the data hint at one. We also study the ‘down-the-barrel’ outflow properties of the AGNs themselves and detect intrinsic NaID absorption in 8/8 systems and intrinsic MgII absorption in 2/2 systems, demonstrating that the AGNs have significant reservoirs of cool gas. We find that 6/8 NaID and 2/2 MgII intrinsic systems contain blueshifted absorption with $\Delta v > 50 \text{ km s}^{-1}$, indicating outflowing gas. The 2/2 intrinsic MgII systems have outflow velocities a factor of ~ 4 higher than the NaID outflow velocities. Our results are consistent with AGN-driven outflows destroying the cool gas within their halos, which dramatically decreases their cool gas covering fraction, while star-burst driven winds are expelling cool gas into their circumgalactic media (CGM). This picture appears contrary to quasar–quasar pair studies which show that the quasar CGM contains significant amounts of cool gas whereas intrinsic gas found ‘down-the-barrel’ of quasars reveals no cool gas. We discuss how these results are complementary and provide support for the AGN unified model.

Key words: —galaxies: ISM, haloes —quasars: absorption lines.

1 INTRODUCTION

Galactic outflows originating in regions of high star formation surface-density and in active galactic nuclei (AGNs) likely play a significant role in regulating the metal content of galaxies and are probably fully responsible for the chemical enrichment of the intergalactic medium (IGM) (e.g. Oppenheimer et al. 2010). Understanding the distribution and extent of the cool gas surrounding galaxies can aid in constraining the metal contribution via winds to the CGM and IGM. Though there are many studies of outflows originating from star-forming galaxies (Tremonti et al. 2007; Zibetti et al. 2007; Martin & Bouché 2009; Weiner et al. 2009; Noterdaeme et al. 2010; Rubin et al. 2010; Steidel et al. 2010; Bordoloi et al. 2011; Coil et al. 2011; Kacprzak & Churchill 2011; Nestor et al. 2011; Ménard & Fukugita 2012; Martin et al. 2012; Rubin et al. 2013; Bordoloi et al. 2013), we are only beginning to understand the effect and distribution of gas surrounding AGNs (e.g. Heckman et al. 2000; Martin 2005; Rupke et al. 2005a,b).

Recent work has shown that large gas reservoirs surround quasars with a covering fraction of 60–80% and a physical extent of 200 kpc (Hennawi et al. 2006; Bowen et al. 2006; Prochaska & Hennawi 2009; Tytler et al. 2009; Farina et al. 2013; Prochaska et al. 2013; Farina et al. 2014), similar to what is observed for inactive field galaxies (Kacprzak et al. 2008; Chen et al. 2010; Nielsen et al. 2013; Churchill et al. 2013a,b). The cool gas surrounding field galaxies, as traced by MgII absorption, exhibits an anisotropic distribution whereby most gas is located along their projected major and minor axes, which is interpreted to be due to accretion and outflows, respectively (Kacprzak et al. 2011b; Bordoloi et al. 2011; Bouché et al. 2012; Bordoloi et al. 2012; Kacprzak et al. 2012). Quasars also exhibit an anisotropic gas distribution possibly caused by the intense AGN-driven ionizing radiation that heats the gas to temperatures of $\sim 10^5 \text{ K}$ and destroys cool gas clouds out to a few hundred kiloparsecs (Chelouche et al. 2008). Prochaska et al. (2013) analyzed 74 quasar–quasar pairs with projected separations of $D < 300 \text{ kpc}$ and showed that, although quasars exhibit a high covering fraction of cool gas as traced by H I and C II, cool gas is rarely detected along the jet (‘down-

* gkacprzak@astro.swin.edu.au

the-barrel') of the quasar itself. They suggest that the background quasar sight-lines intercept gas that is shadowed from the ionizing radiation of the quasar jet. Similar anisotropy has been observed in H I (Hennawi & Prochaska 2007; Prochaska & Hennawi 2009) and Mg II (Bowen et al. 2006; Farina et al. 2013, 2014). The distribution of the CGM of AGNs, like Seyfert galaxies, has yet to be explored.

If the AGN radiation field is responsible for destroying cool gas, then the orientation of the AGN-driven outflows with respect to the background quasar sight-line may dictate the presence, strength and frequency of the absorption. The inclination of the AGN-driven outflows are primarily constrained by the unified AGN model (see Bianchi et al. 2012, and references therein). The type of AGN observed may be dependent on the observers' vantage point, or essentially the AGN dust torus inclination. Quasars and blazars are typically viewed down-the-barrel of the AGN jet (face-on torus), while broad-line Seyfert I objects are viewed at a slightly higher inclination and narrow-line Seyfert IIs are viewed with an edge-on torus. If one were to probe quasars or blazars with background quasars, the dusty torus is in the plane of the sky (face-on and orthogonal to the jet) and provides the maximum cross-section of radiation-shielded extended halo gas, yielding the highest covering fraction of cool halo gas. Therefore, we would expect that the cool gas covering fraction surrounding AGNs should decrease as the inclination of the dusty torus decreases from face-on to edge-on for quasars, Seyfert Is and Seyfert IIs, respectively.

Motivated by the idea that the gas covering fraction of AGNs may change with viewing angle (according to the unified model), we target a sample of 14 narrow-line AGN (Seyfert IIs) to examine their cool CGM gas covering fractions. We target $z \sim 0.15$ AGN so that we are able to detect the Mg II $\lambda\lambda 2796, 2803$ and Na I D $\lambda\lambda 5892, 5897$ absorption doublets from ground-based facilities and we are able to resolve the morphological properties of their host galaxies in ground-based images. We investigate the cool gas covering fractions and azimuthal angle dependencies. We show that AGN exhibit intrinsic absorption, unlike quasars, and we quantify their outflow properties. In Section 2 we present our sample and data reduction. In Section 3, we present the gas covering fractions and azimuthal dependencies. present clear signs of intrinsic (down-the-barrel) cool gas outflows originating from ongoing star-formation rather than the jets and quantify their outflow properties. In Section 4, we discuss what can be inferred from the results and how it arises naturally from the AGN unified model. Concluding remarks are offered in Section 5. Throughout we adopt an $H_0 = 70 \text{ km s}^{-1} \text{ Mpc}^{-1}$, $\Omega_M = 0.3$, $\Omega_\Lambda = 0.7$ cosmology.

2 GALAXY SAMPLE AND DATA ANALYSIS

2.1 Sample Selection

To probe the gas environment around AGN we have searched for AGN that lie in the foreground of background quasars. We cross-correlated a catalogue of $\sim 12,000$ AGN that are spectroscopically classified using SDSS (DR2) spectra (Hao et al. 2005) with spectroscopically classified quasars in SDSS (DR7). Out of the 77 foreground AGN-background quasar pairs identified, we applied the following selection criteria: (1) The projected separations are less than 400 kpc; (2) A redshift separation of $\Delta z > 20,000 \text{ km s}^{-1}$ to avoid confusion between the foreground AGN Mg II absorption and the intrinsic Mg II absorption from the quasar; (3) Both the foreground AGN and the background quasar have a SDSS g-band apparent magnitude of $m_g < 20$; (4) The Mg II absorption occurs redward of the quasar Ly α emission in order to avoid the Ly α forest.

A total of 31 foreground AGN-background quasar pairs meet these selection criteria. We have observed 14 AGN-quasar pairs that were at optimal airmass during our observing runs. The 14 foreground AGN presented here have a redshift range determined by SDSS of $0.12 \leq z \leq 0.22$. Typical redshift errors are $\Delta z = 0.00005$ ($\sim 15 \text{ km s}^{-1}$). The background quasars probe the foreground AGNs over an impact parameter range of $60 \leq D \leq 265 \text{ kpc}$. All 14 objects are narrow-line AGN (Seyfert II).

2.2 AGN & Background Quasar Spectroscopy

The combined wavelength coverage and ultra-blue sensitivity of Keck/LRIS (Oke et al. 1995; Steidel et al. 2004) is ideal for targeting Mg II absorption (Barton & Cooke 2009; Kacprzak et al. 2011a) and Na I D absorption (Rupke et al. 2005) at $z = 0.1 - 0.2$. The Keck/LRIS foreground AGN and background quasar spectra were obtained over three nights; one was obtained in 2009 September and 13 were obtained in two nights in 2010 February. The LRIS slit was oriented such that the background quasar and AGN fell within the slit. Details of the observations are presented in Table 1. We used the LRIS-B/Keck 1200 lines/mm grism, blazed at 3400 \AA , which covers a wavelength range of $2910 - 3890 \text{ \AA}$. We used a $1.0''$ slit that yields a dispersion of 0.24 \AA per pixel and provides a resolution of $\text{FWHM} \sim 1.6 \text{ \AA}$ ($\sim 150 \text{ km s}^{-1}$). Integration times of 1880–5120 seconds were used, depending on the magnitude of the quasar and the foreground AGN redshift, providing 3σ detection limits of $W_r(2796) \sim 0.3 \text{ \AA}$. We concurrently used the LRIS-R/Keck 1200 lines/mm grating blazed at 7500 \AA , set to a central wavelength of 6314 \AA , which covers a wavelength range of $5495 - 7133 \text{ \AA}$. The $1.0''$ slit used yields a dispersion of 0.40 \AA per pixel and provides a resolution of $\text{FWHM} \sim 1.9 \text{ \AA}$ ($\sim 85 \text{ km s}^{-1}$). The spectra were reduced using the standard IRAF packages¹ and were corrected to the vacuum and heliocentric frame.

The quasar spectra were searched for Mg II and Na I D doublet candidates using a detection significance level of 3σ for each doublet member. Detection and significance levels follow the formalism of Schneider et al. (1993) and Churchill et al. (2000a). In addition, intervening and intrinsic Mg II and C IV absorption systems serendipitously identified in the spectra that were not targeted in this survey are listed in Table A1.

Analysis of the absorption profiles was performed using our own graphics-based interactive software that uses the flux values in individual pixels to measure the equivalent widths and the redshift of the Mg II $\lambda 2796$ transition (Churchill & Vogt 2001). Flux weighted absorption velocity widths were measured between the pixels where the equivalent width per resolution element recovers to the 1σ detection threshold (Churchill et al. 1999, 2000a). The redshift for each Mg II and/or Na I D system is computed from the optical depth weighted mean of the absorption profile. The statistical uncertainties in the redshifts range between $0.00001 - 0.00009$ ($\sim 3 - 30 \text{ km s}^{-1}$ co-moving).

¹ IRAF is written and supported by the IRAF programming group at the National Optical Astronomy Observatories (NOAO) in Tucson, Arizona. NOAO is operated by the Association of Universities for Research in Astronomy (AURA), Inc. under cooperative agreement with the National Science Foundation.

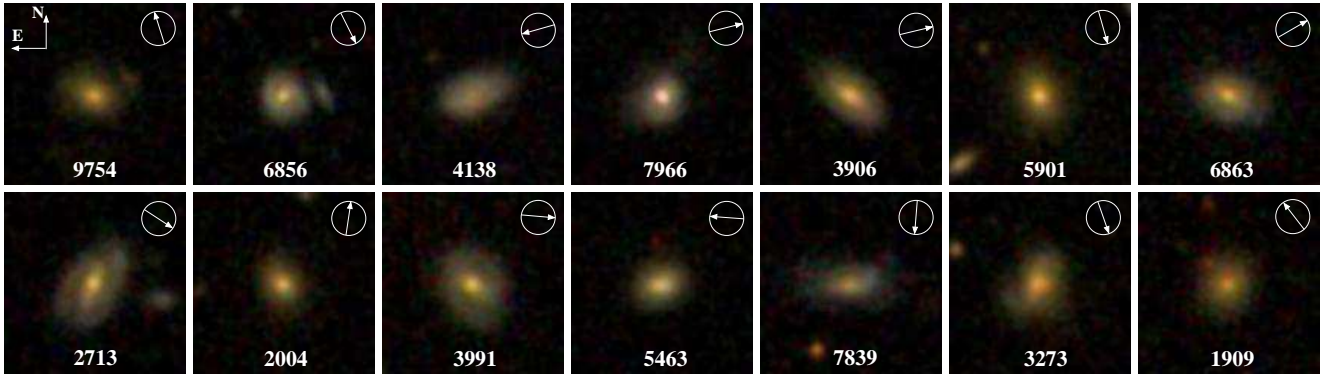


Figure 1. *gri*-band SDSS color images of the 14 foreground narrow-line AGN (Seyfert IIs). The direction of the background quasar sight-line is indicated by the arrow in the upper-right corner of the images. The AGN–quasar separations range between 63–265 kpc. The AGN–quasar pair IDs are located on the bottom of each image. Note that the galaxies tend to have low inclination angles, with average inclination of $i = 51 \pm 12$ degrees.

Table 1. Keck–I/LRIS foreground narrow-line AGN and background quasar observations. The table columns are (1) the quasar name, (2) the quasar RA, (3) the quasar DEC, (4) the AGN and quasar pair name, (5) the quasar redshift, (6) the quasar SDSS *g*-band apparent magnitude, (7) the observation date, and (8) the total integration time in seconds.

SDSS Quasar Name	RA _{QSO} (J2000)	DEC _{QSO} (J2000)	Pair Name	z_{QSO}	m_g	Date (UT)	Exposure (sec.)
SDSS J230632.06+004611.7	23:06:32.06	+00:46:11.78	9754	0.57072	19.8	Sep. 18 2009	1880
SDSS J133216.60+020634.3	13:32:16.60	+02:06:34.39	6856	0.52960	19.2	Feb. 12 2010	3720
SDSS J101133.17+011451.1	10:11:33.17	+01:14:51.17	4138	0.37035	19.9	Feb. 13 2010	4960
SDSS J144732.28+610722.1	14:47:32.28	+61:07:22.19	7966	0.36189	19.6	Feb. 13 2010	4300
SDSS J095105.22+000049.2	09:51:05.22	+00:00:49.29	3906	0.87571	19.3	Feb. 13 2010	4960
SDSS J123844.41+001140.2	12:38:44.41	−00:11:40.22	5901	0.87540	18.8	Feb. 13 2010	3720
SDSS J133248.52+014250.3	13:32:48.52	+01:42:50.35	6863	0.24717	19.3	Feb. 12 2010	5120
SDSS J080626.99+465857.1	08:06:26.99	+46:58:57.12	2713	1.35435	19.7	Feb. 13 2010	4960
SDSS J032605.40−073242.2	03:26:05.40	−07:32:42.23	2004	1.05407	19.6	Feb. 12 2010	3720
SDSS J095701.58+023857.3	09:57:01.58	+02:38:57.32	3991	1.07677	19.3	Feb. 12 2010	3720
SDSS J120210.73+005520.4	12:02:10.73	+00:55:20.44	5463	1.18228	19.4	Feb. 12 2010	3720
SDSS J143729.16+024404.2	14:37:29.16	+02:44:04.21	7839	1.30369	19.8	Feb. 13 2010	3180
SDSS J085755.38+531145.3	08:57:55.38	+53:11:45.32	3273	1.57320	19.6	Feb. 12 2010	3720
SDSS J031531.50−074002.7	03:15:31.50	−07:40:02.71	1909	1.05373	20.0	Feb. 13 2010	2480

Table 2. The foreground AGN and absorption properties. The table columns are (1) the AGN–quasar pair name, (2) the SDSS AGN redshift, (3) the AGN RA, (4) the AGN DEC, (5) the AGN SDSS *g*-band magnitude, (6) the inclination of the host-AGN, (7) The orientations of the quasar sight-lines with respect to the projected major (x -axis, $\Phi = 0$ degrees) and minor (y -axis, $\Phi = 90$ degrees) axis of the AGNs, (7) the projected separation between background quasar and foreground AGN pair, (8) the Mg II $\lambda 2796$ rest-frame equivalent width with 1σ errors or 3σ limits, (8) the Mg II $\lambda 2803$ rest-frame equivalent width with 1σ errors or 3σ limits, (9) the Na I D rest-frame equivalent width limits (3σ), and (10) the Mg II $\lambda 2796$ absorption-line redshift.

Pair Name	z_{AGN}	RA _{AGN} (J2000)	DEC _{AGN} (J2000)	m_g	i (degrees)	Φ (degrees)	D (kpc)	$W_r(2796)$ (Å)	$W_r(2803)$ (Å)	$W_r(\text{NaID})$ (Å)	z_{abs}
9754	0.193216	23:06:31.674	+00:45:53.0	18.7	$54.5^{+5.8}_{-7.2}$	$48.9^{+13.9}_{-9.8}$	62.6	1.05 ± 0.10	0.86 ± 0.10	...	0.193263
6856	0.129467	13:32:18.116	+02:07:19.5	18.0	$34.6^{+24.2}_{-10.5}$	$68.5^{+20.5}_{-22.7}$	117.6	<0.27	<0.27	<0.08	
4138	0.121781	10:11:29.309	+01:15:07.7	18.1	$59.5^{+3.9}_{-4.5}$	$83.5^{+3.7}_{-3.9}$	134.1	<0.23	<0.23	<0.10	
7966	0.136349	14:47:39.330	+61:06:56.1	17.5	$27.3^{+4.3}_{-8.3}$	$38.0^{+31.5}_{-38.7}$	140.2	<0.30	<0.32	...	
3906	0.132690	09:51:09.084	+00:00:35.4	18.0	$62.5^{+3.0}_{-2.6}$	$36.1^{+4.7}_{-3.7}$	141.8	<0.11	<0.11	<0.09	
5901	0.139482	12:38:45.634	−00:10:36.4	18.3	$52.0^{+6.3}_{-6.3}$	$87.4^{+8.3}_{-10.9}$	164.8	<0.13	<0.13	<0.13	
6863	0.165819	13:32:51.879	+01:42:21.2	17.9	$62.6^{+13.6}_{-23.7}$	$35.8^{+16.5}_{-27.2}$	164.8	<0.20	<0.20	...	
2713	0.124705	08:06:32.257	+46:59:48.6	17.8	$58.9^{+3.4}_{-2.6}$	$8.8^{+3.5}_{-3.5}$	168.2	1.37 ± 0.10	1.60 ± 0.09	...	0.124438
2004	0.156050	03:26:06.049	−07:33:46.7	18.6	$48.2^{+4.3}_{-4.9}$	$59.2^{+8.6}_{-6.8}$	176.4	<0.19	<0.19	<0.08	
3991	0.127130	09:57:06.861	+02:39:04.0	17.9	$39.5^{+3.3}_{-4.1}$	$36.2^{+10.8}_{-9.7}$	182.2	<0.17	<0.17	...	
5463	0.163679	12:02:06.463	+00:55:15.6	18.3	$43.4^{+9.8}_{-7.1}$	$68.6^{+10.5}_{-11.6}$	182.6	<0.17	<0.17	<0.07	
7839	0.179098	14:37:28.817	+02:45:08.7	18.3	$67.0^{+2.5}_{-3.3}$	$5.8^{+8.4}_{-7.1}$	198.4	<0.21	<0.21	<0.11	
3273	0.163778	08:57:57.341	+53:13:09.5	18.2	$49.9^{+2.1}_{-7.9}$	$48.9^{+7.8}_{-7.1}$	244.1	<0.28	<0.28	...	
1909	0.198855	03:15:28.231	−07:41:06.2	18.8	$32.3^{+9.5}_{-9.6}$	$41.7^{+16.9}_{-20.9}$	265.2	<0.18	<0.18	<0.11	

2.3 AGN Images & Models

In Figure 1 we show *gri*-band SDSS color images of the 14 foreground AGN. The direction of the background quasar sight-line is indicated by the arrow in the upper-right corner of the images.

The AGN-host galaxy morphological parameters were determined by applying the two-dimensional decomposition fitting program GIM2D (Simard et al. 2002) to the *r*-band images. The image point-spread-function required by GIM2D was derived from nearby stars in each image that were modeled using DAOPHOT (Stetson 1987, 1999).

3 RESULTS

3.1 Transverse Absorption – Covering Fraction

We present the first study of an AGN-selected sample shown in Figure 2 and in Table 2. Our sample of 14 background quasar and foreground AGN pairs probe an impact parameter range of $60 \leq D \leq 265$ kpc with a detection threshold is 0.3 \AA (3σ). For our sample, we find two AGN with absorption detected at $D = 63$ kpc, with $W_r(2796) = 1.1 \text{ \AA}$, and at $D = 168$ kpc, with $W_r(2796) = 1.4 \text{ \AA}$.

In Figure 2 we present “transverse” MgII $\lambda\lambda 2796, 2803$ absorption doublet redshift versus impact parameter for our AGN-selected sample and compare it with quasar-selected samples from other published works. The data presented in Figure 2 have a detection limit of 0.3 \AA at the 3σ level. Tytler et al. (2009) studied 170 quasar–quasar pairs probing distances out to 2 Mpc. Although this sample is large, the majority of quasar–quasar pairs have velocity separations of $\lesssim 20,000 \text{ km s}^{-1}$; it is therefore unclear if the absorption detected is produced by gas surrounding the foreground quasar or by out-flowing gas from the background quasar itself. Only one quasar pair resides within an impact parameter of 300 kpc and is separated by $> 20,000 \text{ km s}^{-1}$. Bowen et al. (2006) and Farina et al. (2013, 2014)² probe 4 and 22 $z \sim 1$ foreground quasars, respectively, for which $D < 200$ kpc and the velocity separation with respect to the background quasars is greater than $20,000 \text{ km s}^{-1}$.

In Figure 3 we present the covering fraction profiles for AGNs (this work), galaxies (Nielsen et al. 2013) and quasars (Farina et al. 2013, 2014). The covering fractions for each sample are determined per impact parameter bin, matching the bins of Nielsen et al. (2013). The plotted value indicates the mean D per bin. The covering fraction errors for each AGN, galaxy, quasar datasets are derived from binomial statistics (Gehrels 1986).

As found by Farina et al. (2014), the covering fractions of quasars are higher than those of isolated galaxies, which is likely due to the richness and extent of the CGM around quasar-host galaxies. This higher MgII covering fraction is consistent with the high CII covering fraction ($\sim 50\%$) found for quasars (Prochaska et al. 2013). However, AGN may exhibit similar or possibly lower covering fractions as compared to field galaxies for $100 \leq D \leq 200$ kpc.

Notwithstanding the obviously poor statistics at $D < 100$ kpc, with one data point (not included on the plot), the data are likely consistent with previous works that AGN-type objects and galaxies have a high covering fraction for $D < 100$ kpc.

² We have recomputed 3σ detection limits for the quoted 2σ limits of Farina et al. (2013, 2014) and removed systems where revised 3σ limits exceed 0.3 \AA .

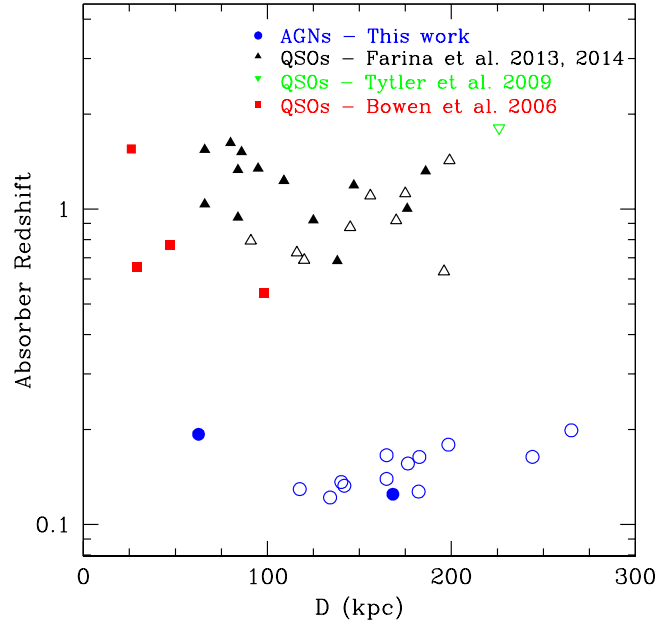


Figure 2. Known MgII absorption from quasar–quasar pairs (represented by squares and triangles) and foreground AGN–quasar pairs (represented by circles). The filled symbols are detected absorbers and the open symbols are non-detections with 3σ equivalent width limits of $< 0.3 \text{ \AA}$ for all four samples.

For 7 of the 14 quasar–AGN pairs, the spectra cover the NaID absorption doublet. However, no NaID was detected down to a 3σ equivalent width threshold of 0.13 \AA , which provides further evidence for no cold gas surrounding the AGNs.

3.2 Transverse Absorption – AGN orientations

In Figure 4, we show the relative position of the quasar sight-lines with respect to the host AGN projected major ($\Phi = 0$ degrees) and minor ($\Phi = 90$ degrees) axes. The solid line represents a typical half opening-angle determined for galactic-scale winds and AGN outflows of 50 degrees (Hjelm & Lindblad 1996; Veilleux et al. 2001; Walter et al. 2002; Müller-Sánchez et al. 2011; Bordoloi et al. 2012; Kacprzak et al. 2012; Martin et al. 2012). Note that most sight-lines probe within the expected region for outflowing gas.

We attempted to determine if there is an azimuthal dependence for the MgII gas covering fraction shown in Figure 4. Since the azimuthal angle for each quasar varies in accuracy and can subtend into several azimuthal angle bins, we apply the method of Kacprzak et al. (2012) whereby we represent the measured azimuthal angles and their uncertainties as uni-variate asymmetric Gaussians, which creates an azimuthal angle probability distribution function (PDF) for each galaxy. Combining the PDFs for all absorbers and non-absorbers produces a mean PDF as a function of the azimuthal angle.

In Figure 4, we present the binned mean azimuthal angle (Φ) PDF for the 2 absorbing and 12 non-absorbing galaxies and their covering fractions as a function of the azimuthal angle. The combined PDFs have been area-normalized to the total number of galaxies in each sub-sample. The covering fraction is computed for each azimuthal bin. The errors in the covering fractions are com-

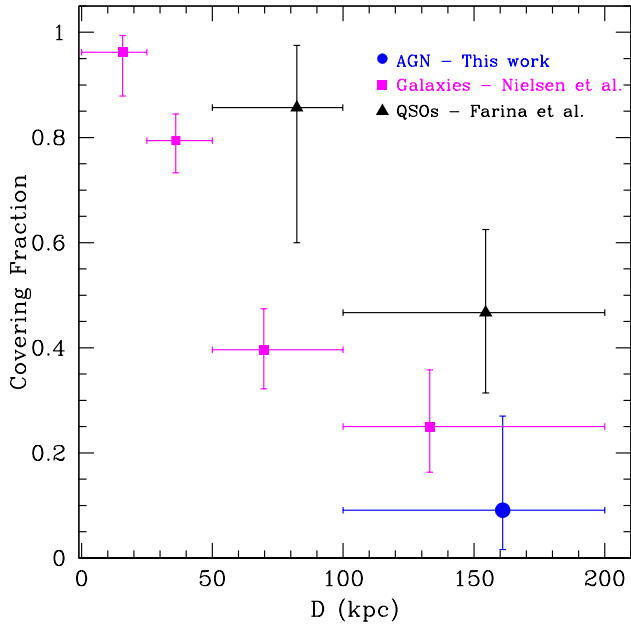


Figure 3. The radial covering fraction profiles for AGN (this work), inactive field galaxies (Nielsen et al. 2013) and quasars (Farina et al. 2013, 2014). All datasets have 3σ equivalent width limits of $> 0.3 \text{ \AA}$. The data points are located at the mean of the impact parameter distribution for each bin. AGNs have covering fractions that are consistent with field galaxies for $100 \leq D \leq 200 \text{ kpc}$. We have excluded our one datapoint at $D < 100 \text{ kpc}$ from this plot since the errors are significantly larger and is consistent with both galaxies and quasars.

puted using binomial statistics (Gehrels 1986). The data are suggestive that there could be an excess of absorbers along the galaxy projected major axis ($\Phi = 0$ degrees) compared to the minor axis ($\Phi = 90$ degrees). However, the current sample size is insufficient to determine statistically if such a geometric dependence exists given the binomial error distributions.

3.3 Transverse Absorption – Gas Kinematics

In Figure 5, we present the two detected absorption systems. The normalized flux of the MgII $\lambda\lambda 2796, 2803$ doublet is plotted with respect to the AGN velocity zero-point. The strongest absorber (ID 2713) is the system at $D = 168 \text{ kpc}$ and $z_{abs} = 0.124438$. This absorber has a MgII rest-frame equivalent width of $W_r(2796) = 1.4 \text{ \AA}$ and a velocity offset of -71 km s^{-1} blueward of the AGN redshift. The quasar sight-line probes the AGN along the projected major axis. The absorber has a full velocity width spanning 272 km s^{-1} .

The absorber at $D = 63 \text{ kpc}$ and $z_{abs} = 0.193263$ (ID 9754) has a $W_r(2796) = 1.1 \text{ \AA}$ and a velocity offset of 12 km s^{-1} redward of the AGN redshift with a full velocity width spanning 355 km s^{-1} . This absorber is located near the projected minor axis of the galaxy.

The transverse absorption velocity offsets for these two systems, relative to the AGN systemic velocities, are small and not suggestive of outflows (e.g., Kacprzak et al. 2010a).

3.4 Line-of-sight outflows

The ionization potential of NaID (5.14 eV) results in a peak in absorption strength in the atmospheres of cool K–M stars (see

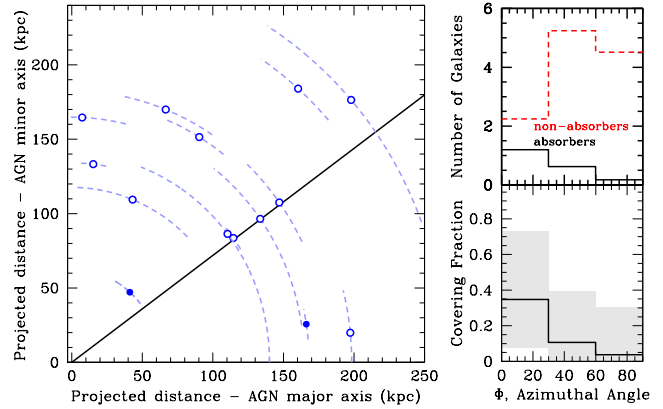


Figure 4. (left) The orientations of the quasar sight-lines with respect to the projected major (x-axis, $\Phi = 0$ degrees) and minor (y-axis, $\Phi = 90$ degrees) axis of the AGNs. The filled symbols are detected MgII absorbers and the open symbols are non-detections with 3σ equivalent width limits of $< 0.3 \text{ \AA}$. The 1σ error-bars are determined from GIM2D model errors in determining the galaxy major axis position angle with respect to the quasar sight-line. The solid line represents a 50 degree half-opening angle typically found for AGN outflows. (right, top) The binned azimuthal angle mean probability distribution function for 2 absorbing (solid line) and 12 non-absorbing AGN (dashed line) produced using the technique described in Kacprzak et al. (2012). The area of the histograms is normalized to the total number of galaxies in each sub-sample. (right, bottom) The azimuthal dependence of the covering fraction with shaded regions providing 1σ binomial errors.

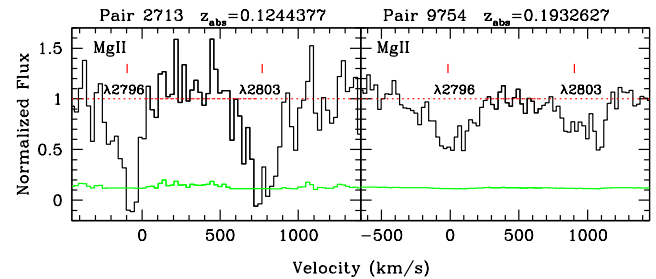


Figure 5. Two MgII $\lambda\lambda 2796, 2803$ absorption profiles associated with foreground AGNs at impact parameters of $D = 168 \text{ kpc}$ and $D = 63 \text{ kpc}$ from left to right, respectively. The velocity zero points are fixed to the redshifts of the AGN. The horizontal line (red) at unity is the continuum fit while the solid lines (green) are the 1σ error spectra.

Jacoby et al. 1984). In addition, it is further absorbed by cool gas within, and surrounding, galaxies. For example, NaID has been detected as entrained gas within galactic-scale outflows with velocities ranging between $100\text{--}1000 \text{ km s}^{-1}$ (e.g. Heckman et al. 2000; Martin 2005; Rupke et al. 2005a,b). These outflows are measured by observing velocity offsets between galaxy nebular emission lines and ISM absorption lines.

In Figure 6, we present the NaID absorption doublet for 8 of the 14 AGNs. Not all 14 absorption profiles are presented since some are blended with strong sky features, such as the $6860\text{--}6890 \text{ \AA}$ B-band, while others were not recorded because they reside outside the spectral and spatial range of the spectrograph. The flux normalized spectra are plotted at the systemic velocity of the AGN, determined from emission-lines, relative to the NaID $\lambda 5897$ line. We further show two intrinsic MgII absorption systems where the signal-to-noise ratio was sufficient to provide a detection. Note that

there is no significant evidence for MgII being detected in emission. Qualitatively, in most cases, there appears to be blueshifted outflows with maximum velocities of $\sim 500 \text{ km s}^{-1}$.

To quantify the outflow velocities of the gas, we modeled our data with a procedure similar to that of Rupke et al. (2005a). Least-squares Gaussian deblending was performed (using the program FITTER; Churchill et al. 2000a) to estimate the equivalent widths, velocity widths, and velocity centroids of component structures in the absorption profiles. We fit the minimum number of Gaussian velocity components to the absorption profiles that was well-constrained/required by the data; typically one-to-two components was sufficient to model each absorption system. For four of the NaID systems, we were required to simultaneously model the HeI $\lambda 5876$ emission-line using a single component set to the systemic velocity of the galaxy. In all cases we fixed the NaID and MgII doublet ratios to unity to avoid unphysical models.

Our fit results are presented in Table 3 and Figure 6. The red and blue tick-marks in the figure indicate the red and blue components of the doublet required in the fit. Only for three NaID systems (and both MgII systems) were two doublets required by the data.

Following Rupke et al. (2005b), we adopt the definition that $\Delta v > 50 \text{ km s}^{-1}$ is outflowing wind material. From Table 3, we find that 6/8 NaID systems contain blueshifted absorption with $\Delta v > 50 \text{ km s}^{-1}$, indicating outflows with velocities ranging between 55 to 125 km s^{-1} . In 2/8 systems, one has redshifted absorption and the other has absorption near the systemic velocity. For all 6 outflow objects, we find a mean Doppler parameter of $b = 220 \pm 70 \text{ km s}^{-1}$, which is consistent with the range of values derived by Rupke et al. (2005) for 20 Seyfert II galaxies at $z = 0.148^{+0.14}_{-0.07}$ having $b = 232^{+244}_{-119} \text{ km s}^{-1}$.

Rupke et al. (2005) also define the maximum outflow velocity to be the central velocity of the most blueshifted component minus half its FWHM: $\Delta v_{\text{max}} = \Delta v - \text{FWHM}/2$. The Δv_{max} for our sample is listed in Table 3 and we find a mean value for the 6 wind systems of $\Delta v_{\text{max}} = 277 \pm 87 \text{ km s}^{-1}$, which is also consistent with, but smaller than, the values determined by Rupke et al. (2005) of $\Delta v_{\text{max}} = 456^{+330}_{-191} \text{ km s}^{-1}$.

We have applied generalized Kendall and Spearman rank correlation tests between the outflow properties with the galaxy inclination angle. We only find suggestive trends with inclination and the outflow equivalent width (2.1σ) and inclination and b (1.7σ). Additional galaxies are required to test the significance of these correlations.

The two MgII absorption systems also exhibit high velocity outflowing gas, higher than what is detected for NaID in the same systems. The blueshifted velocity offset for the bluest MgII components for both systems is $\sim 400 \text{ km s}^{-1}$ from the AGN systemic velocity, a factor of more than ~ 4 higher than the NaID outflows. The Doppler parameters are consistent with those found for the NaID. However, Δv_{max} is a factor of two higher than those of the NaID systems. This suggests that MgII traces warmer gas and is more sensitive to outflowing material than the NaID absorption.

4 DISCUSSION

It is clear that there are large H I/metal reservoirs surrounding quasars because their gas covering fractions are 60–80% out to 200 kpc (Hennawi et al. 2006; Bowen et al. 2006; Prochaska & Hennawi 2009; Tytler et al. 2009; Farina et al. 2013; Prochaska et al. 2013; Farina et al. 2014). Farina et al. (2014) show that the covering fraction of MgII absorption around quasars is

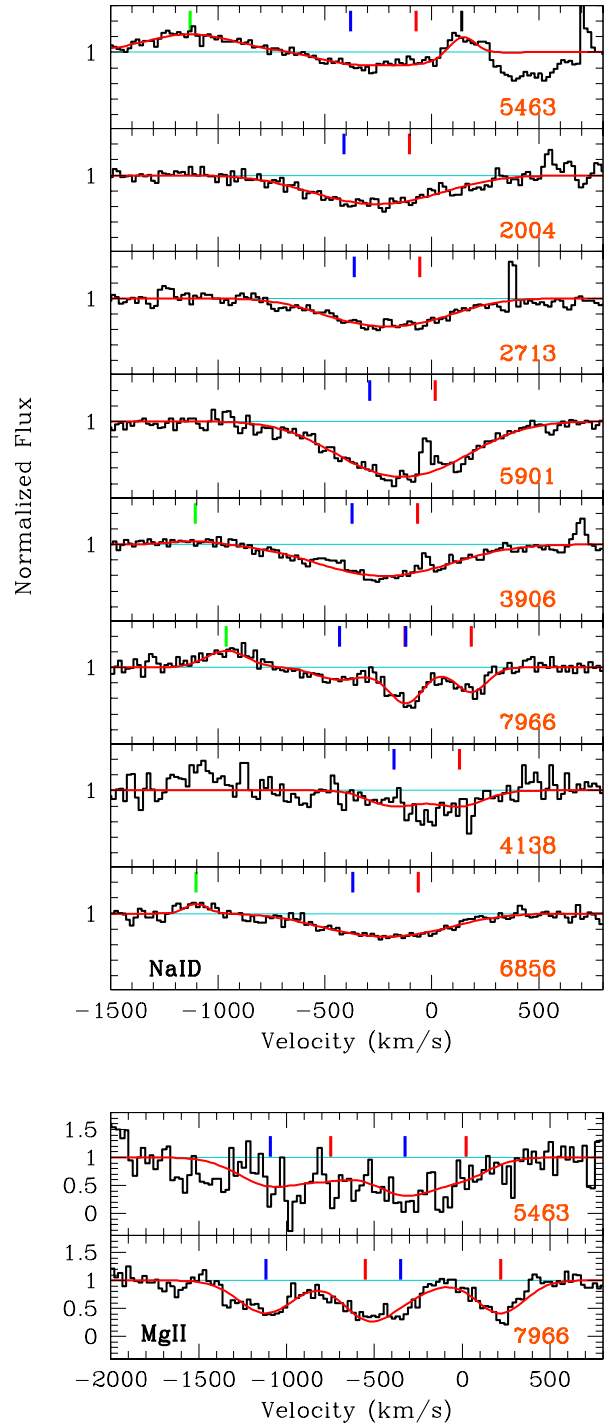


Figure 6. NaID (top) and MgII (bottom) absorption intrinsic (down-the-barrel) to the AGN host galaxies. The flux-normalized spectra (black) are shown with respect to the AGN systemic velocity with $v = 0 \text{ km s}^{-1}$, set to the NaID $\lambda 5876$ line (top) and the MgII $\lambda 2803$ line (bottom). The wind model fitted to the data is shown along with red and blue tick-marks that indicate the red and blue components of the doublet required in the fit. In four cases, a fit to the HeI emission-line was required (green tick mark). The AGN name is listed in the bottom right corner of each panel. The results of the model fits are shown in Table 3.

Table 3. The foreground AGN down-the-barrel absorption properties. The table columns are (1) the AGN–quasar pair name, (2) the ion measured, (3) the rest-frame equivalent width, (4) the cloud velocity offset from AGN systemic velocity, (5) the Doppler parameter or velocity width of the cloud, (6) the maximum outflow velocity defined as $\Delta v_{\max} = \Delta v - \text{FWHM}/2$.

Pair	Ion	W_r (Å)	Δv (km s ^{−1})	b (km s ^{−1})	Δv_{\max} (km s ^{−1})
6856	NaID	2.05±0.13	−62±16	311±30	−218±22
4138	NaID	1.48±0.13	130±17	209±28	26±22
7966	NaID	1.14±0.04	185±3	103±4	...
	NaID	0.81±0.05	−125±10	151±13	−201±12
	MgII	3.73±0.10	161±10	194±8	...
	MgII	2.60±0.11	−406±8	222±10	−547±62
3906	NaID	3.02±0.15	−68±16	358±28	−247±21
5901	NaID	5.22±0.17	16±9	342±17	−155±12
2713	NaID	2.43±0.09	−55±17	294±33	−202±24
2004	NaID	2.69±0.14	−104±15	339±27	−274±20
5463	NaID	1.02±0.17	−73±44	209±62	−178±54
	MgII	2.11±0.30	−37±7	212±11	...
	MgII	6.31±1.01	−382±55	330±58	−517±9

more elevated than that found for field galaxies. We find here that AGN have lower covering fractions, $0.09^{+0.18}_{-0.08}$, than quasars, $0.47^{+0.16}_{-0.15}$, and possibly lower than galaxies, $0.25^{+0.11}_{-0.09}$ between $100 \leq D \leq 200$ kpc.

The main difference between galaxies, AGN, and quasars is the mass and energy output of their central massive black holes. Chelouche et al. (2008) modeled the distribution of cool gas around quasars and concluded that conical AGN-driven winds could heat the gas to temperatures of $\sim 10^5$ K and could photo-ionize and photo-evaporate cool MgII gas clouds out to a few hundred kiloparsecs. This is consistent with the observed anisotropic distribution of gas around quasars (e.g. Farina et al. 2014). Quasar–quasar pairs exhibit high transverse covering fractions while intrinsic MgII absorption in a quasar’s own spectrum is rarely seen (e.g. Hennawi & Prochaska 2007; Prochaska & Hennawi 2009; Farina et al. 2013; Prochaska et al. 2013; Farina et al. 2014). Farina et al. (2014) report zero intrinsic MgII absorption detections in 26 quasar spectra. This is consistent with our observations of intrinsic MgII absorption in the quasar, documented in Table A1, where we show that the background quasars only yield intrinsic MgII absorption in 1/5 objects ($W_r(2796) < 0.14$ Å, 3σ). However, for our foreground AGN sample, we detect 2/2 objects with intrinsic absorption along with 8/8 systems containing intrinsic NaID absorption (shown in Figure 6). This result indicates that cool gas clouds intrinsic to the AGN are not destroyed by the ionizing radiation originating central massive black holes and suggests that the observed anisotropic distribution of gas around quasars and AGN is consistent with the AGN unification scheme (e.g. Urry & Padovani 1995) since gas within AGN-driven winds is heated to high temperatures, while the CGM remains unaffected outside of the wind region.

Given that AGN outflows are roughly conical, with half opening angles ranging between $\sim 30 - 70$ degrees (Hjelm & Lindblad 1996; Veilleux et al. 2001; Müller-Sánchez et al. 2011), one might expect an anisotropic distribution of cool gas surrounding the AGN: absorption would be detected outside the jet region and there would be a lack of absorption inside the jet region. We do not find a statistically significant azimuthal angle dependence for the MgII covering fraction around the AGN hosts, though a possible hint of one may exist. A caveat to our geometric assumption, contrary to

starburst-driven winds, is that AGN outflow jets (Seyfert Is and IIs) measured at radio wavelengths are oriented almost randomly relative to the major axis of the host galaxy (e.g. Kinney et al. 2000; Gallimore et al. 2006). Simulations have shown that offsets between the jet orientation with respect to the angular momentum of the disk can be caused by galaxy mergers or by instabilities (gravitational or accretion) in isolated disks (Hopkins et al. 2012). This could be why we do not find a strong trend between the covering fraction and azimuthal angle. Thus, if there is a trend between covering fraction and orientation, it could be diluted by the jet/disk offsets and thus detecting a statistically significant trend (if it exists) would require a larger sample than the one we present here.

It is well known that most optically-selected AGN also host nuclear starbursts that produce starburst-driven winds (e.g. Veilleux et al. 2001; Rupke et al. 2005). Our host galaxies have a median inclination of $i = 51 \pm 12$ degrees and thus, if there are star formation driven winds, we may observe them via blueshifted absorption-line outflows (see Fig 6). In 6/8 systems we find NaID outflows with $\Delta v > 50$ km s^{−1}, the maximum blueshifted velocities reaching up to $\Delta v_{\max} = 277 \pm 87$ km s^{−1}. These values are consistent with the measurements made using NaID absorption for 20 AGN Seyfert IIs at a similar redshift by Rupke et al. (2005). It is likely that these outflows are primarily due to star-formation driven winds because the AGN winds are perpendicular to the line-of-sight, although there could be a combination of both (Veilleux et al. 2001). Rupke et al. (2005) find that the star formation rates of Seyfert IIs range between $118^{+151}_{-66} M_{\odot} \text{ yr}^{-1}$, with outflow masses and outflow rates of $\log(M/M_{\odot}) = 8.8 \pm 0.5$ and $dM/dt = 18^{+50}_{-13} M_{\odot} \text{ yr}^{-1}$, respectively. Given the consistencies between the outflow properties of Rupke et al. (2005) and our sample, we expect that our AGNs could have similar outflow masses and rates produced in starburst-driven winds.

In two cases, shown in Figure 6, we also detect MgII absorption outflowing from the AGN at speeds ~ 4 times higher than found for NaID. All of the detected NaID and MgII absorption indicates the presence of gas reservoirs with most of them outflowing from the host galaxy. However, even though we find that the AGN hosts contain significant amounts of cool gas, we do not observe it in their halos in MgII absorption as probed by the background quasars.

Given the high covering fraction found for quasars and the lack of metal-line absorption within intrinsic down-the-barrel quasar spectra, which would be equivalent to looking down the jet of an AGN, is highly suggestive that the cool gas is ionized by the jets. Furthermore, we find evidence that cool gas is indeed being ejected at a few hundred km s^{−1} from the AGN. However we do not observe significant amounts of absorption around them. This adds credence to that idea that the AGN-driven winds may be destroying the MgII, consistent with the AGN unified model (Urry & Padovani 1995).

5 CONCLUSIONS

We have performed a detailed study of the cool gas covering fraction, traced by MgII absorption, surrounding narrow-line AGN (Seyfert IIs) using background quasar sight-lines. We analyzed 14 AGN–quasar pairs with the foreground AGN having a redshift range of $0.12 \leq z \leq 0.22$. The background quasars probe cool halo gas surrounding the foreground AGNs over an impact parameter range of $60 \leq D \leq 265$ kpc. We further study the ‘down-the-barrel’ outflow properties of the AGNs themselves.

Our mains results can be summarized as follows:

(i) We find that AGN appear to have lower covering fractions between $100 \leq D \leq 200$ kpc, $0.09^{+0.18}_{-0.08}$, than quasars, $0.47^{+0.16}_{-0.15}$, and possibly lower than galaxies, $0.25^{+0.11}_{-0.09}$. We do not find a statistically significant azimuthal angle dependence for the MgII absorption covering fraction around the AGNs, though there could be a possible hint of one. More AGN–quasar pairs are required to demonstrate the azimuthal angle dependence or lack thereof and to test rigorously test for differences in the covering fractions.

(ii) AGN intrinsic NaID absorption lines detected in 8/8 systems indicate that the AGN hosts have significant reservoirs of cool gas. This is validated by the 2/2 intrinsic MgII absorption lines systems also detected.

(iii) We find that 6/8 intrinsic NaID systems contain blueshifted absorption with $\Delta v > 50$ km s⁻¹, indicating outflows. For all 6 outflow objects, we find a mean Doppler parameter of $b = 220 \pm 70$ km s⁻¹ and a maximum outflow velocity of $\Delta v_{max} = 277 \pm 87$ km s⁻¹, both consistent with the range of values computed by Rupke et al. (2005) for 20 Seyfert II galaxies at a similar redshift.

(iv) The 2/2 intrinsic MgII absorption systems also exhibit high velocity outflowing gas and are a factor of than ~ 4 higher than the NaID outflows and the Δv_{max} being a factor of two higher than those of the NaID systems. This is suggestive that MgII traces warmer gas that is more sensitive to outflowing material than the NaID absorption.

Our results are consistent with AGN-driven winds ionizing the cool gas, which dramatically decreases the cool $T \sim 10^4$ K gas covering fraction of AGN. Our observations also show that star-burst driven winds are expelling cool gas into the CGM. This picture is consistent with results from quasar–quasar pair studies. Previous quasar–quasar studies have found that intrinsic cool gas down-the-barrel is non-existent while their halos contain significant amounts of cool gas. Both these results are complementary and provide support for the AGN unified model.

ACKNOWLEDGMENTS

We thank the anonymous referee for providing insightful comments and improving the paper. MTM and JC thank the Australian Research Council for Discovery Project grant DP130100568 and Future Fellowship grant FT130101219 which supported this work. We thank W.M. Keck Observatory, which is operated as a scientific partnership among the California Institute of Technology, the University of California and the National Aeronautics and Space Administration. Keck Observatory was made possible by the generous financial support of the W.M. Keck Foundation. Data was also obtained from the Sloan Digital Sky Survey (SDSS). Funding for the SDSS and SDSS-II has been provided by the Alfred P. Sloan Foundation, the Participating Institutions, the National Science Foundation, the U.S. Department of Energy, the National Aeronautics and Space Administration, the Japanese Monbukagakusho, the Max Planck Society, and the Higher Education Funding Council for England. The SDSS Web Site is <http://www.sdss.org/>. The SDSS is managed by the Astrophysical Research Consortium for the Participating Institutions. The Participating Institutions are the American Museum of Natural History, Astrophysical Institute Potsdam, University of Basel, University of Cambridge, Case Western Reserve University, University of Chicago, Drexel University, Fermilab, the Institute for Advanced Study, the Japan Participation Group, Johns Hopkins University, the Joint Institute for Nuclear Astrophysics, the Kavli Institute for Particle Astrophysics and Cosmology, the

Korean Scientist Group, the Chinese Academy of Sciences (LAM-OST), Los Alamos National Laboratory, the Max-Planck-Institute for Astronomy (MPIA), the Max-Planck-Institute for Astrophysics (MPA), New Mexico State University, Ohio State University, University of Pittsburgh, University of Portsmouth, Princeton University, the United States Naval Observatory, and the University of Washington.

REFERENCES

- Barton, E. J., & Cooke, J. 2009, *AJ*, 138, 1817
 Bianchi, S., Maiolino, R., & Risaliti, G. 2012, *Advances in Astronomy*, 2012,
 Bordoloi, R., Lilly, S. J., Hardmeier, E., et al. 2013, arXiv:1307.6553
 Bordoloi, R., Lilly, S. J., Kacprzak, G. G., & Churchill, C. W. 2012, arXiv:1211.3774
 Bordoloi, R., Lilly, S. J., Knobel, C., et al. 2011, *ApJ*, 743, 10
 Bowen, D. V., Hennawi, J. F., Ménard, B., et al. 2006, *ApJ*, 645, L105
 Bouché, N., Hohensee, W., Vargas, R., Kacprzak, G. G., et al. 2012, *MNRAS*, 426, 801
 Chelouche, D., Ménard, B., Bowen, D. V., & Gnat, O. 2008, *ApJ*, 683, 55
 Chen, H.-W., Helsby, J. E., Gauthier, J.-R., Shectman, S. A., Thompson, I. B., & Tinker, J. L. 2010, *ApJ*, 714, 1521
 Churchill, C. W., Mellon, R. R., Charlton, J. C., Jannuzi, B. T., Kirhakos, S., Steidel, C. C., & Schneider, D. P. 2000a, *ApJS*, 130, 91
 Churchill, C. W., Nielsen, N. M., Kacprzak, G. G., & Trujillo-Gomez, S. 2013, *ApJ*, 763, L42
 Churchill, C. W., Rigby, J. R., Charlton, J. C., & Vogt, S. S. 1999, *ApJS*, 120, 51
 Churchill, C. W., Trujillo-Gomez, S., Nielsen, N. M., & Kacprzak, G. G. 2013, arXiv:1308.2618
 Churchill, C. W., & Vogt, S. S. 2001, *AJ*, 122, 679
 Coil, A. L., Weiner, B. J., Holz, D. E., et al. 2011, *ApJ*, 743, 46
 Farina, E. P., Falomo, R., Decarli, R., Treves, A., & Kotilainen, J. K. 2013, *MNRAS*, 429, 1267
 Farina, E. P., Falomo, R., Scarpa, R., et al. 2014, arXiv:1403.5559
 Gallimore, J. F., Axon, D. J., O’Dea, C. P., Baum, S. A., & Pedlar, A. 2006, *AJ*, 132, 546
 Gehrels, N. 1986, *ApJ*, 303, 336
 Hao, L., Strauss, M. A., Tremonti, C. A., et al. 2005, *AJ*, 129, 1783
 Hennawi, J. F., & Prochaska, J. X. 2007, *ApJ*, 655, 735
 Hennawi, J. F., Prochaska, J. X., Burles, S., et al. 2006, *ApJ*, 651, 61
 Heckman, T. M., Lehnert, M. D., Strickland, D. K., & Armus, L. 2000, *ApJS*, 129, 493
 Hjelm, M., & Lindblad, P. O. 1996, *A&A*, 305, 727
 Hopkins, P. F., Hernquist, L., Hayward, C. C., & Narayanan, D. 2012, *MNRAS*, 425, 1121
 Jacoby, G. H., Hunter, D. A., & Christian, C. A. 1984, *ApJS*, 56, 257
 Kacprzak, G. G., & Churchill, C. W. 2011a, *ApJ*, 743, L34
 Kacprzak, G. G., Churchill, C. W., Barton, E. J., & Cooke, J. 2011a, *ApJ*, 733, 105
 Kacprzak, G. G., Churchill, C. W., Ceverino, D., Steidel, C. C., Klypin, A., & Murphy, M. T. 2010, *ApJ*, 711, 533
 Kacprzak, G. G., Churchill, C. W., Evans, J. L., Murphy, M. T., & Steidel, C. C. 2011b, *MNRAS*, 416, 3118
 Kacprzak, G. G., Churchill, C. W., Steidel, C. C., & Murphy, M. T. 2008, *AJ*, 135, 922
 Kacprzak, G. G., Churchill, C. W., & Nielsen, N. M. 2012, *ApJ*, 760, L7
 Kinney, A. L., Schmitt, H. R., Clarke, C. J., et al. 2000, *ApJ*, 537, 152
 Martin, C. L. 2005, *ApJ*, 621, 227
 Martin, C. L., & Bouché, N. 2009, *ApJ*, 703, 1394
 Martin, C. L., Shapley, A. E., Coil, A. L., et al. 2012, *ApJ*, 760, 127
 Ménard, B., & Fukugita, M. 2012, *ApJ*, 754, 116
 Müller-Sánchez, F., Prieto, M. A., Hicks, E. K. S., et al. 2011, *ApJ*, 739, 69
 Nielsen, N. M., Churchill, C. W., & Kacprzak, G. G. 2013, *ApJ*, 776, 115
 Nestor, D. B., Johnson, B. D., Wild, V., et al. 2011, *MNRAS*, 412, 1559

- Noterdaeme, P., Srianand, R., & Mohan, V. 2010, MNRAS, 403, 906
- Oke, J. B., et al. 1995, PASP, 107, 375
- Oppenheimer, B. D., Davé, R., Kereš, D., et al. 2010, MNRAS, 406, 2325
- Prochaska, J. X., & Hennawi, J. F. 2009, ApJ, 690, 1558
- Prochaska, J. X., Hennawi, J. F., & Simcoe, R. A. 2013, ApJ, 762, L19
- Rubin, K. H. R., Prochaska, J. X., Koo, D. C., et al. 2013, arXiv:1307.1476
- Rubin, K. H. R., Prochaska, J. X., Koo, D. C., Phillips, A. C., & Weiner, B. J. 2010, ApJ, 712, 574
- Rupke, D. S., Veilleux, S., & Sanders, D. B. 2005a, ApJS, 160, 87
- Rupke, D. S., Veilleux, S., & Sanders, D. B. 2005b, ApJS, 160, 115
- Rupke, D. S., Veilleux, S., & Sanders, D. B. 2005, ApJ, 632, 751
- Schneider, D. P., et al. 1993, ApJS, 87, 45
- Simard, L., Willmer, C. N. A., Vogt, N. P., Sarajedini, V. L., Philips, A. C., Weiner, B. J., Koo, D. C., Im, M., Illingworth, G. D., & Faber, S. M. 2002, ApJS, 142, 1
- Steidel, C. C., Erb, D. K., Shapley, A. E., Pettini, M., Reddy, N., Bogosavljević, M., Rudie, G. C., & Rakic, O. 2010, ApJ, 717, 289
- Steidel, C. C., Shapley, A. E., Pettini, M., et al. 2004, ApJ, 604, 534
- Stetson, P. B. 1987, PASP, 99, 191
- Stetson, P. B. 1999, "Users Manual for DAOPHOT II"
- Tremonti, C. A., Moustakas, J., & Diamond-Stanic, A. M. 2007, ApJ, 663, L77
- Tytler, D., Gleed, M., Melis, C., et al. 2009, MNRAS, 392, 1539
- Urry, C. M., & Padovani, P. 1995, PASP, 107, 803
- Veilleux, S., Shopbell, P. L., & Miller, S. T. 2001, AJ, 121, 198
- Walter, F., Weiss, A., & Scoville, N. 2002, ApJ, 580, L21
- Weiner, B. J., et al. 2009, ApJ, 692, 187
- Zibetti, S., Ménard, B., Nestor, D. B., Quider, A. M., Rao, S. M., & Turnshek, D. A. 2007, ApJ, 658, 161

APPENDIX A: ADDITIONAL INTRINSIC AND FOREGROUND ABSORBERS

We document additional intrinsic and foreground $\text{Mg II } \lambda\lambda 2796, 2803$ doublet and $\text{C IV } \lambda\lambda 1548, 1550$ doublet absorption systems detected in our survey. For intrinsic quasar absorption line systems we list the 3σ detection limit for an unresolved line located at the redshift of the quasar.

Table A1. Additional intrinsic and foreground Mg II $\lambda\lambda 2796, 2803$ doublet and C IV $\lambda\lambda 1548, 1550$ doublet absorption systems. The table columns are (1) the AGN name, (2) the AGN redshift, (3,4) the C IV $\lambda 1548$ and $\lambda 1548$ rest-frame equivalent width, (5) the C IV $\lambda 1548$ absorption-line redshift, (6,7) the Mg II $\lambda 2796$ and $\lambda 2803$ rest-frame equivalent width, (8) and (10) the Mg II $\lambda 2796$ absorption-line redshift.

Name	z_{QSO}	$W_r(1548)$ [Å]	$W_r(1551)$ [Å]	z_{abs}	$W_r(2796)$ [Å]	$W_r(2803)$ [Å]	z_{abs}
9754	0.57072
2004	1.05407	<0.15	<0.15	...	<0.05	<0.05	...
3273	1.57320
3991	1.07677	<0.08	<0.08
5463	1.18228	0.26±0.02	0.19±0.02	1.1793724	0.24±0.01	0.13±0.01	1.1799584
6856	0.52960
		0.58±0.04	0.56±0.04	0.2732928
6863	0.24717	<0.08	<0.08	...
1909	1.05373	<0.14	<0.14	...
2713	1.35435	0.90±0.03	0.58±0.03	1.3550805
		0.79±0.03	0.66±0.03	1.1954113
3906	0.87571
4138	0.37035	<0.08	<0.08	...
5901	0.87540
7839	1.30369	0.98±0.03	0.92±0.03	1.3140370
		0.48±0.03	0.28±0.03	1.3035057
7966	0.36189